Nonlinear Dyn
https://doi.org/10.1007/s11071-025-10906-w

RESEARCH

Critical manifolds in the dynamics of a two-wheel model of an automobile

Alois Steindl · Johannes Edelmann · Manfred Plöchl

Received: 30 September 2024 / Accepted: 15 January 2025

Abstract Insight into steering and stability properties of automobiles in critical driving conditions is essential to advance driver assist systems and autonomous driving functions. To study the dynamic properties of an automobile with rear-wheel drive, methods of geometric singular perturbation theory are applied to a planar two-wheel vehicle model. Following a branch of periodic solutions bifurcating from the steady state of the vehicle at the limits of handling, a behaviour similar to a cycle near a homoclinic orbit is observed. The periodic orbit spends most of its period on a segment with an almost constant sideslip angle and slowly varying velocity. This behaviour can be explained by the nearby existence of a critical manifold consisting of a family of stationary solutions and a heteroclinic orbit connecting two points of this critical manifold. For slightly perturbed parameter values the critical manifold is replaced by a slow manifold with very slow dynamics, which governs the dynamics along the observed slow segment. The critical manifold and the heteroclinic orbit are calculated numerically, and good agreement with the derived approximations is obtained.

A. Steindl (✉) · J. Edelmann · M. Plöchl
Institute for Mechanics and Mechatronics, TU Wien, Getreidemarkt 9, 1060 Vienna, Austria
e-mail: Alois.Steindl@tuwien.ac.at

J. Edelmann
e-mail: Johannes.Edelmann@tuwien.ac.at

M. Plöchl
e-mail: Manfred.Ploechl@tuwien.ac.at

Keywords Singular perturbation theory · Invariant manifolds · Limit cycles · Heteroclinic orbit · Vehicle handling · Nonlinear handling characteristics · Powerslide · Drifting

Mathematics Subject Classification 34D15 · 34C37 · 34C45

1 Introduction

Vehicle models for numeric simulation of the dynamics of automobiles have become increasingly complex in recent years. The aim to simulate real dynamic behaviour brought engineers to include a high level of detail in their vehicle models, facilitated by the application of multibody dynamics software. Basic vehicle models are popular in control design, however, they are still indispensable to reveal and understand basic dynamic phenomena.

Handling characteristics of automobiles have been investigated over many decades, leading to a deep insight into the steering and stability properties of automobiles [10,11] as an example of early contributions. Considering extreme and critical driving conditions, however, there are still phenomena, well-known from observations, which deserve closer attention.

Inspired from observations in rallye sports, measurements of large sideslip manoeuvres have been presented in Abdulrahim [1], Velenis et al. [17]. On the basis of a simple nonlinear four-wheel vehicle model

Published online: 28 January 2025

with rear-wheel drive and a tyre model, that comprises the mutual influence of longitudinal and lateral tyre forces, up to four different steering angles have been numerically identified for steady-state cornering at the same velocity and cornering radius [4]. These results have been supported by measurements. Stability analysis in Edelmann and Plöchl [3] reveals the unstable nature of two of these steady-state solutions including the powerslide motion, also denoted drifting. The powerslide of an automobile with rear-wheel drive is defined in Edelmann and Plöchl [3] as a steady-state cornering motion with a large sideslip angle of the vehicle, considerably large traction forces and a steering angle towards the outside of the curve (countersteering), see also Fig. 1. A study on the post-critical behaviour of the powerslide motion is conducted in Edelmann et al. [5] applying bifurcation and continuation methods. It is shown that after loss of stability, assuming fixed driver controls, i.e. steering angle and drive torque, a transient motion of the vehicle may result in steady-state cornering conditions tacking a very narrow circular path, or stable limit cycles. Measurements confirm the findings of the theoretical study. These conditions are known from motorsports and are denoted 'donuts' by vehicle dynamicists.

In Della Rossa et al. [2] published an analysis of possible equilibria for different vehicle handling and tyre characteristics and configurations with a two-degree-of-freedom two-wheel vehicle and a 'magic formula' type tyre model [12]. By systematically analysing all the equilibria and their bifurcations for both oversteering vehicles and understeering vehicles [12], a catalogue of the system behaviours, including the transition from and to limit cycles, is derived. Applying a similar vehicle model, the sensitivity of tyre parameters and driver input quantities w.r.t. the appearance and characteristics of limit cycles in automobiles are investigated in Pauwelussen [13]. Two conditions for the appearance of limit cycles are found: The ratio of the lateral peak friction potential between the front and rear tyres/axles, and a dedicated interval of front steering angle. In Steindl et al. [15], the loss of stability and the post-critical behaviour of oversteering vehicles are studied for a rear-wheel drive two-wheel vehicle model. A Hopf-type loss of stability is identified, and the Canard phenomenon is observed in the bifurcation analysis for small variations of the steering angle and the drive torque close to the saturation of the front and rear tyres.

Applying a four-degree-of-freedom two-wheel vehicle model, the influence of the peak friction coefficient w.r.t the sliding friction coefficient in the tyre characteristics on periodic motions is studied in Steindl et al. [16] for understeering vehicles. Results using the 'classical', monotonous brush tyre model [12], are compared to results obtained using a modified brush tyre model with decaying friction force potential for large slips, and to findings using a magic formula type tyre model. Both the modified brush tyre model and the magic formula type tyre model deliver similar results, where, compared to the monotonous brush tyre model, in particular, the orbit of the periodic motions differs and a switching behaviour close to one of the Hopf points may be noticed.

In this paper, the nonlinear handling and stability properties of a planar two-wheel vehicle model with rear-wheel drive are investigated. After introducing the vehicle model in Sect. 2, findings on the characteristics of the handling diagram shown in Edelmann et al. [4] are confirmed and periodic solutions bifurcating from the steady-state powerslide branch and a steady-state branch with a small radius of curvature of the trajectory of the centre of gravity of the vehicle in the road plane are presented in Sect. 3. These periodic solutions are discussed thoroughly in Sect. 4 applying the geometric singular perturbation theory. Concluding remarks on the findings and an outlook are given in Sect. 5.

2 System model

In this study the dynamics of a planar two-wheel vehicle model with rear-wheel drive displayed in Fig. 1 is investigated. The equations of motion are given by Steindl et al. [16],

$$\begin{aligned} m\dot{v}\cos\beta - m(\dot{\psi}+\dot{\beta})v\sin\beta &= F_{xR} - F_{yF}\sin\delta_F, && \text{(1a)}\\ m\dot{v}\sin\beta + m(\dot{\psi}+\dot{\beta})v\cos\beta &= F_{yR} + F_{yF}\cos\delta_F, && \text{(1b)}\\ I_\psi\ddot{\psi} &= l_F F_{yF}\cos\delta_F - l_R F_{yR}, && \text{(1c)}\\ I_\omega\dot{\omega}_R &= M_R - r_R F_{xR}. && \text{(1d)} \end{aligned}$$

The degree of freedom of the system is represented by the velocity v, the vehicle sideslip angle β, the yaw rate $\dot{\psi}$, and the angular velocity of the driven rear wheel ω_R. The control variables are given by the front steering

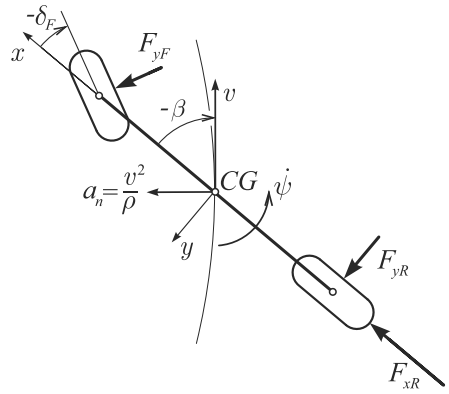

Fig. 1 Two-wheel vehicle model shown in powerslide condition, with state variables v, β, $\dot{\psi}$, ω_R (not depicted) and control parameters δ_F and M_R (not depicted)

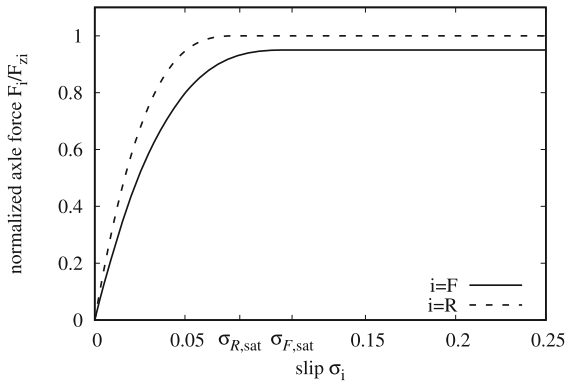

Fig. 2 Normalized tyre characteristics of front and rear tyre

angle δ_F and the drive torque M_R. These control variables are considered to be constant inputs in this study.

The mass and inertia w.r.t. the vertical axis of the vehicle are denoted m and I_ψ, respectively and the inertia of the rear tyre is denoted I_ω. The horizontal tyre forces F_{yF}, F_{xR}, F_{yR} depend on the tyre slips σ_i, $i \in \{F, R\}$, and are described by the brush tyre model,

$$F_i = \mu_i F_{zi} f(|\sigma_i|/\sigma_{i,\text{sat}}) \operatorname{sign}(\sigma_i),$$

where $\sigma_{i,\text{sat}}$ represents the tyre slips at the onset of the saturation of the tyre forces and

$$f(s) = \begin{cases} 3s - 3s^2 + s^3 & \text{for } s \le 1 \\ 1 & \text{for } s > 1 \end{cases} \tag{2}$$

The normalized tyre characteristics $\mu_i f(\sigma_i/\sigma_{i,\text{sat}})$ for the chosen tyre parameters with $\mu_F = 0.95$ and $\mu_R = 1$ are displayed in Fig. 2, characterising an understeering vehicle.

It is assumed that the longitudinal slip σ_{xF} vanishes since no drive forces are applied at the front wheel,

Table 1 Parameters of vehicle and simplified tyre/axle model ([16])

Parameter	Abbr.	Value	Unit
Vehicle mass	m	2000	kg
Vehicle yaw inertia	I_ψ	2650	kg m^2
Axle inertia	I_ω	6	kg m^2
Front axle position $\overline{CG\,F}$	l_F	1.45	m
Rear axle position $\overline{CG\,R}$	l_R	1.50	m
Effective tyre radius	r_R	0.35	m
Front axle slip stiffness	$2c_{pF}a_F^2$	$2.6{\cdot}10^5$	N
Rear axle slip stiffness	$2c_{pR}a_R^2$	$3.6{\cdot}10^5$	N
Max. friction coefficient	μ_F, μ_R	0.95, 1	–
Saturated slip values	$\sigma_{F,\text{sat}}$	0.109	–
	$\sigma_{R,\text{sat}}$	0.0804	–

and the inertia of the front wheel may be disregarded. Therefore, the angular velocity of the front wheel is governed by the longitudinal velocity v_{xcF} of the contact point, and the lateral tyre slip σ_{yF} is given by

$$\sigma_{yF} = \frac{v_{ycF}}{|v_{xcF}|}, \tag{3}$$

with

$$\begin{pmatrix} v_{xcF} \\ v_{ycF} \end{pmatrix} = \begin{pmatrix} \cos\delta_F & \sin\delta_F \\ \sin\delta_F & -\cos\delta_F \end{pmatrix} \begin{pmatrix} v\cos\beta \\ v\sin\beta + l_F\dot{\psi}. \end{pmatrix} \tag{4}$$

Since instances where v_{xcF} becomes negative may be observed, corresponding to a backward rotation of the front wheel, the absolute value in (3) avoids a discontinuity.

For the slip at the rear wheel, the formulas from Steindl et al. [15] are used:

$$\sigma_{xR} = \frac{-v_{xcR}}{v_R} \quad \text{and} \quad \sigma_{yR} = \frac{-v_{ycR}}{v_R} \tag{5}$$

with

$$\begin{pmatrix} v_{xcR} \\ v_{ycR} \end{pmatrix} = \begin{pmatrix} v\cos\beta - r_R\omega_R \\ v\sin\beta - l_R\dot{\psi} \end{pmatrix},$$

$$\sigma_R = \sqrt{\sigma_{xR}^2 + \sigma_{yR}^2}, \quad \text{and } v_R = r_R\omega_R.$$

For the numerical results, the parameters of an understeering vehicle shown in Table 1 are applied.

3 Derivation of steady-state and periodic solutions

The handling diagram for the considered vehicle model driving with a constant radius of curvature of $\rho = 50$ m

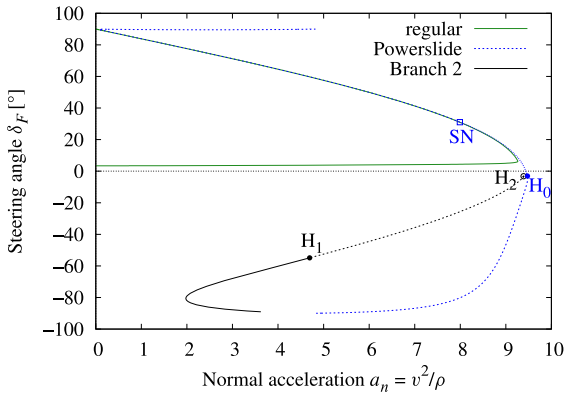

Fig. 3 Handling diagram for the radius of curvature $\rho = 50\,\mathrm{m}$ ('regular' and 'Powerslide' branch), and 'Branch 2' related to the 'Powerslide' branch, with varying radius of curvature ρ. Solid lines refer to stable sections of the respective branches; dashed lines refer to unstable sections of the branches

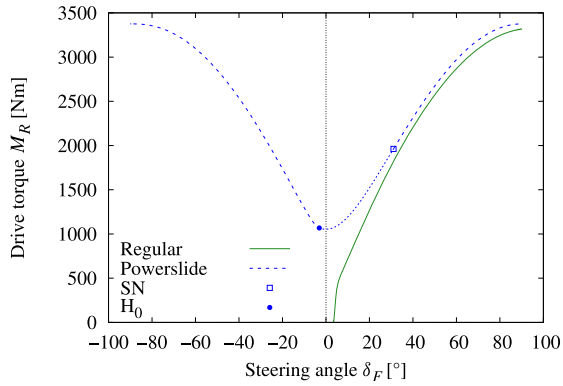

Fig. 4 Relation between steering angle δ_F and drive torque M_R for the radius of curvature $\rho = 50\,\mathrm{m}$

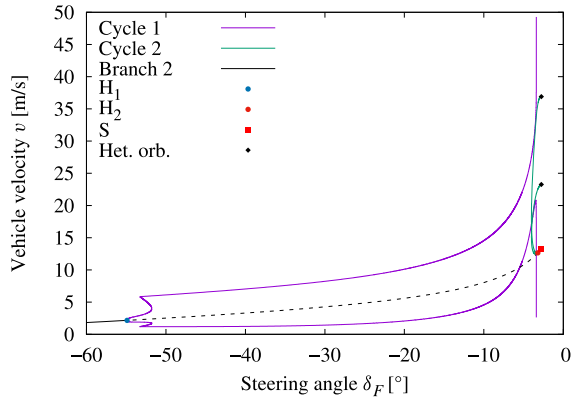

Fig. 5 Periodic solutions bifurcating from the Hopf bifurcation points H_1 and H_2

on the road plane is displayed in Fig. 3. It shows the relation between the normal acceleration $a_n = v^2/\rho$ and the steering angle δ_F for steady-state cornering. Since an understeering vehicle is considered in this study, the 'regular' branch, which corresponds to regular cornering, is stable. A second family of mostly unstable steady-state cornering conditions is called 'powerslide' [3,5], or 'drifting'. At this branch the front wheel points to the outside of the curve, opposite to regular driving. Since for steady-state cornering the vehicle velocity v and yaw rate $\dot{\psi}$ satisfy the relation

$$v = \rho\dot{\psi}, \tag{6}$$

two free parameters are necessary to obtain a family of steady states. In this study, the constant control inputs δ_F and M_R are selected as free parameters. These control inputs vary along the regular branch and powerslide branch depicted in Fig. 3 according to Fig. 4, $M_R = M_R(\delta_F)$. Since in powerslide condition the tyre forces are quite large, also the required drive torque M_R is large even for small absolute values of the steering angle δ_F.

By simulating the dynamics starting close to an unstable point of the powerslide branch and assuming fixed control parameters δ_F and M_R, trajectories are obtained that converge to either a different steady state with a very small radius of curvature ρ of the trajectory of the centre of gravity of the vehicle in the road plane, or to a periodic motion. Also the sense of rotation is reversed. The new steady states are denoted 'Branch 2' in Fig. 3. Along Branch 2, two Hopf points H_1 and H_2 are found. In between these points the steady states are unstable.

The periodic solutions bifurcating from the Hopf points H_1 and H_2 are displayed in Figs. 5, 6 together with the respective steady-state branch. The square denoted 'S' indicates the point where the friction potential of the font tyre is saturated for both the steady-state powerslide branch and Branch 2: Along the powerslide branch the slip σ_{yF} becomes $\sigma_{F,\mathrm{sat}}$, while on Branch 2 $\sigma_{yF} = -\sigma_{F,\mathrm{sat}}$.

For the periodic solutions, the minimal and maximal values of the velocity v are drawn. It may be observed that the branches of the periodic solutions, 'Cycle 1' and 'Cycle 2', are not connected. Close to $\delta_F = -3.4°$ the diameter of the branch Cycle 1 grows strongly and $v_{\min}$ approaches zero while the period becomes very large. The branch Cycle 2 bifurcates from the Hopf point H_2 at Branch 2 in Fig. 3, encounters a limit point

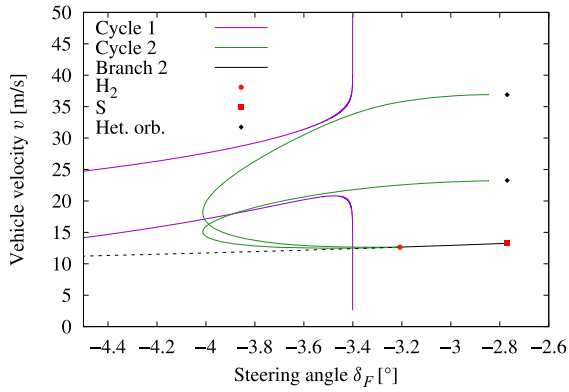

Fig. 6 Enlarged view of Fig. 5 close to H_2

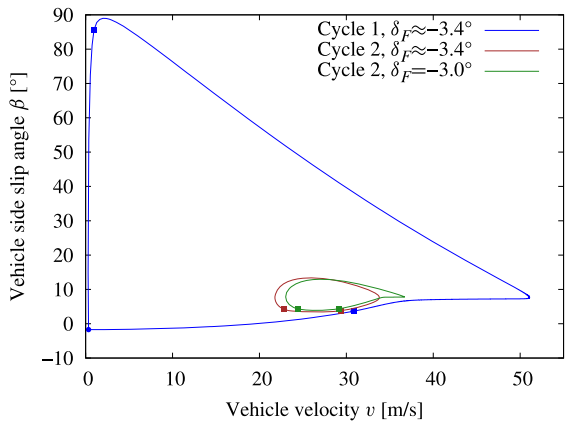

Fig. 7 Phase portrait of periodic solutions in the (v, β)-plane

of cycles and approaches a periodic solution with an infinitely long period. The related limiting solution, which corresponds to the heteroclinic trajectory discussed in Sect. 4, is indicated in Figs. 5, 6 by black diamonds.

Three phase portraits of these periodic solutions are presented in Fig. 7. The orbit depicted in blue colour corresponds to a large amplitude cycle close to the endpoint of the branch Cycle 1 in Fig. 6, while the brown orbit shows the periodic solution for the same parameter values of δ_F and M_R on the branch Cycle 2. The green orbit refers to a periodic solution near to the right end of Cycle 2. Both the blue and green orbits contain an almost horizontal segment close to the right 'nose'. Along this segment, the sideslip angle $\beta(t)$ remains almost constant, while the velocity $v(t)$ increases slowly, as depicted in Fig. 8 for the green orbit. The structure of these solutions is investigated in Sect. 4.

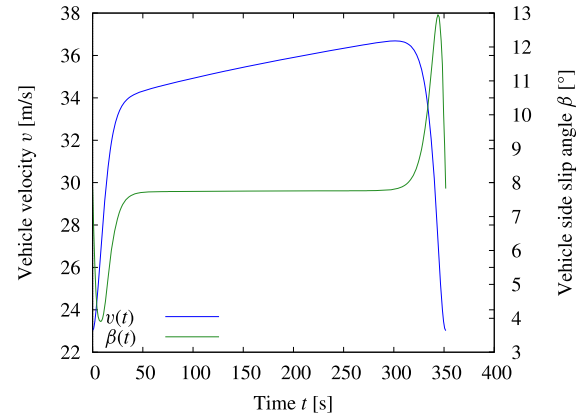

Fig. 8 Evolution of $v(t)$ and $\beta(t)$ for the periodic solution at $\delta_F = -3°$ depicted in green color in Fig. 7

The squares in Fig. 7 indicate the onset and the end of the section of the orbit, where the front tyre is operated at large slips $\sigma_F \geq \sigma_{F,\mathrm{sat}}$, i.e. the friction potential of the tyre is saturated. The circles indicate the onset and the end of the section, where the rear tyre is operated at large slips. Considering the blue orbit, the friction potential of the front tyre and the rear tyre is not saturated in the left segment of the orbit between the squares and circles, respectively. Please note that the onset of the saturation of both the front tyre and the rear tyre almost coincide on the blue orbit at $v \approx 30$ m/s and $\beta \approx 3°$. On the orbits depicted in brown and green colour in Fig. 7, the friction potential of the rear tyre is always saturated, whereas the friction potential of the front tyre is unsaturated only in the short, almost horizontal segments.

4 Explanation of the 'long period' periodic solutions using geometric singular perturbation theory

The equations (1) representing the dynamics of the vehicle contain several sources of singular behaviour:

- The tyre forces strongly depend on the slip between the tyres and the road in both longitudinal and lateral directions. For small slips, the system becomes singularly perturbed with the tyre stiffness as large parameter. A 'Canard explosion' after the onset of periodic solutions at a Hopf bifurcation point is observed in Steindl et al. [15].

- For very small steering angles and drive torques ('free rolling' of the vehicle) the variables v and ω_R become almost linearly dependent. This leads to a very small, stable eigenvalue.
- The brush tyre model is not valid if the velocity of the tyres' contact point vanishes [12].
- When both tyres operate in the saturated range ($\sigma_i > \sigma_{i,\mathrm{sat}}$), $i \in \{F, R\}$, of the brush tyre model, a zero eigenvalue occurs, because the magnitude of the tyre forces becomes constant, and only the direction depends on the state variables. Also applying more sophisticated tyre models, e.g. a 'magic formula' type tyre model [12], the asymptotic behaviour for large slips ($\sigma_i > \sigma_{i,\mathrm{sat}}$) can cause similar phenomena. The dynamics caused by this singularity will be explored subsequently.

4.1 Critical manifold in the saturated range of the tyres

Along the almost horizontal segments of the periodic solutions in Fig. 7 both tyres operate in the saturated range $\sigma_i > \sigma_{i,\mathrm{sat}}$, therefore the magnitude of the tyre forces is given by the constant values $F_i = \pm\mu_i F_{zi}$ for the brush model and near these segments there exists a one-dimensional family of steady-state solutions of the equations derived from (1)

$$F_{yF}\sin(\beta-\delta_F) + F_{xR}\cos\beta + F_{yR}\sin\beta = 0, \quad (7a)$$

$$-mv\dot{\psi} + F_{yF}\cos(\delta_F-\beta) + F_{yR}\cos\beta - F_{xR}\sin\beta = 0, \quad (7b)$$

$$l_F F_{yF}\cos\delta_F - l_R F_{yR} = 0, \quad (7c)$$

$$M_R - r_R F_{xR} = 0. \quad (7d)$$

for a certain value of M_R.

For the lateral tyre force at the front wheel $F_{yF} = \pm\mu_F F_{zF}$ with $F_{zF} = mgl_R/(l_F+l_R)$ is obtained. The observed solution is given by $F_{yF} = -\mu_F F_{zF}$. From (7c) it follows that

$$F_{yR} = l_F F_{yF}\cos\delta_F / l_R,$$

from which the remaining tyre force is found

$$F_{xR} = \pm\sqrt{\mu_R^2 F_{zR}^2 - F_{yR}^2} \quad (8)$$

with $F_{zR} = mgl_F/(l_F+l_R)$.

Since in the considered parameter range $M_R > 0$, the positive value according to (7d) is chosen.

Since

$$\frac{F_{xR}}{F_{yR}} = \gamma_R := \frac{v_{xcR}}{v_{ycR}},$$

the ratio γ_R must be constant along the branch of steady-state solutions.

The steady-state sideslip angle β can now be obtained from (7a)

$$\tan\beta = \frac{F_{yF}\sin\delta_F - F_{xR}}{F_{yF}\cos\delta_F + F_{yR}}.$$

From (7b) a further equation for the remaining state variables v and $\dot{\psi}$ is obtained. Eqn. (7d) can now be solved for M_R, it yields a constant value for constant values of γ_R. As γ_R is already determined by (8), (7d) cannot be used to solve for any state variable.

If M_R satisfies (7d), the equations (7a-c) determine a one-dimensional manifold of steady-state solutions, the so-called 'critical manifold' $\mathscr{M}_c$ ([7]).

In the following

$$M_R = M_R^0 + \varepsilon, \quad \text{with } M_R^0 = r_R F_{xR}, \quad (9)$$

is assumed, where ϵ denotes a small perturbation parameter and F_{xR} is given by (8).

Numerical calculations show that along $\mathscr{M}_c$ two eigenvalues of the Jacobian are stable, one is unstable and one eigenvalue becomes zero because the steady-state solutions form a continuous curve and are not isolated. The shape of the periodic solutions displayed in Fig. 7 suggests, that points on $\mathscr{M}_c$ are connected by a heteroclinic orbit, which leaves a point $P_1 \in \mathscr{M}_c$ along the unstable manifold and returns to another point $P_2 \in \mathscr{M}_c$ along the stable manifold. The existence of a family of such orbits, which depends on the steering angle δ_F, has been established numerically by solving a corresponding boundary value problem. The respective method is explained in the appendix. For long periods the periodic solution follows the heteroclinic solution and the critical manifold between P_2 and P_1. For $\varepsilon \neq 0$ the points along $\mathscr{M}_c$ are not steady-state anymore and according to Fenichel [6], Kuehn [7] the presence of a 'slow manifold' $\mathscr{M}_s$ is expected nearby, which takes on the role of saddle points for homoclinic orbits. Along $\mathscr{M}_s$ the state variables evolve slowly and show the same saddle point-like stability properties in transversal direction as the stationary solutions along $\mathscr{M}_c$: along the stable manifold neighboring trajectories converge to $\mathscr{M}_s$, whereas they diverge from it along the unstable manifold. During their slow evolution the periodic solutions approach $\mathscr{M}_s$ exponentially close.

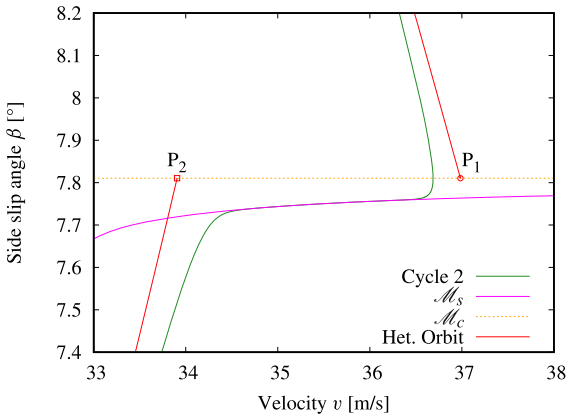

Fig. 9 Periodic solution, slow manifold $\mathscr{M}_s$, heteroclinic orbit and critical manifold $\mathscr{M}_c$ for $\delta_F = -3°$.

Figure 9 shows a detailed view of the periodic solution (green), the corresponding slow manifold $\mathscr{M}_s$ (magenta), the heteroclinic orbit (red) and the critical manifold $\mathscr{M}_c$ for $\delta_F = -3°$. For the periodic solution and $\mathscr{M}_s$ the control variable M_R is chosen according to Fig. 4, whereas for $\mathscr{M}_c$ and the heteroclinic orbit it is given by the value M_R^0 according to (9).

4.2 Dynamics along the slow manifold $\mathscr{M}_s$

The control parameters δ_F and M_R for the periodic solutions are selected according to the powerslide branch for steady-state cornering with radius of curvature $\rho = 50$m. The 'long' periodic solutions occur when the slip σ_{yF} at the front tyre for the steady-state motion approaches saturation, while the slip σ_R at the rear tyre is far beyond the initial saturation. Let δ_{Fs} and M_{Rs} denote the corresponding values of the input parameters, which can numerically be calculated by stating the additional equation

$$|\sigma_{yF}| = \sigma_{F,\mathrm{sat}}. \tag{10}$$

For δ_F slightly smaller than δ_{Fs}, $|\sigma_{yF}| < \sigma_{F,\mathrm{sat}}$ is observed and to first order

$$\sigma_{F,\mathrm{sat}} - \sigma_{yF} = c_\sigma \Delta\delta_F = c_\sigma(\delta_{Fs} - \delta_F),$$

where the factor c_σ is obtained by differentiating (3) w.r.t. δ_F, taking into account that also the steady-state values of v, β and $\dot\psi$ in (4) depend on δ_F.

Since $f(1) = 1$, $f'(1) = 0$, $f''(1) = 0$, and $f'''(1) = 6$, the tyre force at the front wheel satisfies

$$\begin{aligned} F_{yF} &= \mu_F F_{zF} f(|\sigma_{yF}|/\sigma_{F,\mathrm{sat}})\,\mathrm{sign}(\sigma_{yF}) \\ &\approx -\mu_F F_{zF}\left(1 - f'''(1)(c_\sigma\Delta\delta_F)^3/6\right) \\ &= -\mu_F F_{zF}\left(1 - \mathscr{O}(\Delta\delta_F)^3\right). \end{aligned}$$

For the tyre force at the rear wheel the estimates

$$\begin{aligned} F_{yR} &= F_{yR}^0(1 - \mathscr{O}(\Delta\delta_F)^3), \\ F_{xR} &= F_{xR}^0(1 + \mathscr{O}(\Delta\delta_F)^3), \end{aligned}$$

are obtained, where the quantities F_{yR}^0 and F_{xR}^0 denote the forces at the critical manifold.

Inserting these findings into (7d) results in

$$M_R = M_R^0 + \mathscr{O}(\Delta\delta_F)^3, \tag{11}$$

such that $\varepsilon = \mathscr{O}(\Delta\delta_F)^3$. Along the slow manifold the speed of the trajectory is of order $\mathscr{O}(\varepsilon)$. Hence, the periodic solutions converge to the heteroclinic orbit when δ_F converges to δ_{Fs}. The period grows with $1/\Delta\delta_F^3$, as it can be seen in Fig. 12.

According to Kuehn [7] the slow manifold $\mathscr{M}_s$ is ε-close to $\mathscr{M}_c$ and the velocities along the slow manifold are of order $\mathscr{O}(\varepsilon)$. The typical dynamics are discussed in Kuehn [7] and can be guessed from Fig. 7: For $\varepsilon = 0$ there exists a heteroclinic orbit, which starts and ends at different points P_1 and P_2 on $\mathscr{M}_c$. For $\varepsilon \neq 0$ a periodic trajectory is expected, which approximates the heteroclinic orbit and slowly evolves along $\mathscr{M}_s$ between P_2 and P_1. If ε approaches zero, the period T of the periodic solution goes to infinity. Along the heteroclinic solution and sufficiently far from the steady-state points P_1 and P_2 the transition time is almost constant, while it takes $\mathscr{O}(1/\varepsilon)$ time units to travel from P_2 back to P_1 and $\mathscr{O}(\log(1/\varepsilon))$ units to enter and leave the vicinity of the slow manifold. For small values of $\Delta\delta_F$ the expression $\mathscr{O}(1/\Delta\delta_F)^3$ dominates the estimate for the periodic solution.

The behavior along the periodic solution is quite similar to a homoclinic orbit for a saddle point, except that the slow dynamics take place close to $\mathscr{M}_s$. A comparison between periodic solutions and the limiting heteroclinic orbit is shown in Fig. 10. Figure 11 displays the corresponding road trajectory of the centre of gravity of the vehicle for the periodic orbit in the road plane. Along the slow manifold the vehicle velocity v and the radius of cornering $\rho = v/\dot\psi$ grow slowly, and the vehicle moves along a spiral.

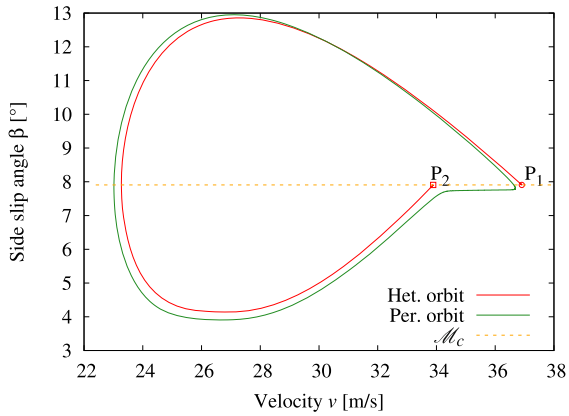

Fig. 10 Periodic and heteroclinic orbits in the (v, β)-plane for $\delta_F = -3°$ (periodic orbit) and $\delta_F = \delta_{Fs} \approx -2.77°$ ($\mathscr{M}_c$ and heteroclinic orbit), respectively

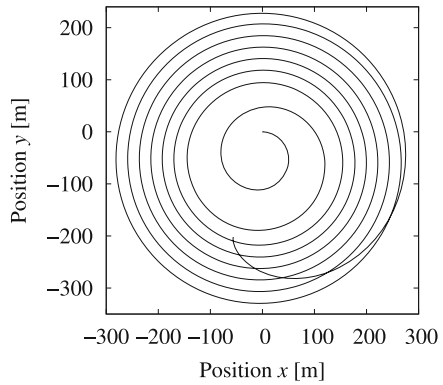

Fig. 11 Vehicle trajectory for the periodic solution at $\delta_F = -3°$ depicted in green color in Fig. 10

4.3 Second branch of heteroclinic orbits

As shown in Fig. 3 there exists also a Hopf bifurcation point H_0 along the powerslide branch. The periodic solutions bifurcating from H_0 show a similar behaviour as those bifurcating from H_2. After passing a limit point cycle (LPC), they approximate a heteroclinic orbit connecting steady-state points on a critical manifold, which differs from the previous critical manifold: The steady-state friction force F_{yF} at the front wheel now reaches the positive value $\mu_F F_{zF}$, also F_{yR} changes its sign due to (7c), the value of F_{xR} is the same as before. Due to (7a) the side slip angle β takes a different value, very close to its value on the powerslide branch.

Figure 12 displays a bifurcation diagram for the branches of periodic solutions bifurcating from the Hopf bifurcation points H_2 and H_0 in the $(\delta_F, \sqrt[3]{1/T})$

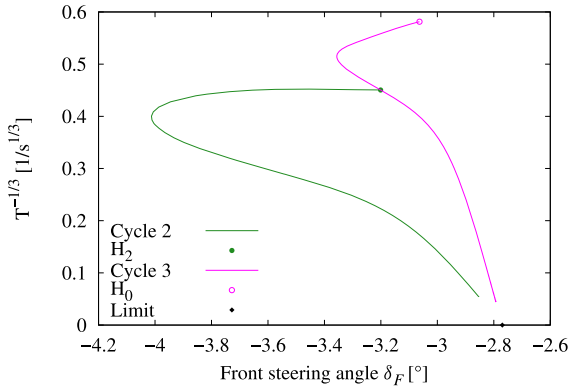

Fig. 12 Bifurcation diagrams for the periodic solutions bifurcating at the Hopf points H_2 and H_0

parameter plane. Both branches end up at the limit point with $\delta_F = \delta_{Fs}$ and $T = \infty$. The periodic solutions in the (v, β)-plane for $\delta_F = -3°$ are shown in Fig. 13 together with the heteroclinic solutions for $\delta_F = \delta_{Fs}$.

For details on the numerical calculation of the periodic and heteroclinic solutions please refer to the Appendix.

5 Summary and outlook

In this manuscript, the handling and stability behaviour of a planar two-wheel vehicle model with rear-wheel drive has been investigated. The occurrence of a family of periodic solutions converging to a heteroclinic solution connecting two points on a critical manifold has been explained. These periodic solutions arise when the tyre slip in the steady-state solution reaches the maximum friction potential of the front tyre, which is associated with the post-critical behaviour of the powerslide motion in automobiles [5]. To derive these results, methods of geometric singular perturbation theory [7], have been applied.

To investigate the impact of the decaying friction force potential for large slips of typical rubber tyres on the dynamic behaviour of the vehicle, future work will include a corresponding tyre model. Preliminary investigations suggest the emergence of solution patterns that should also be tractable using geometric singular perturbation theory. The presented research addressed the characteristics of the uncontrolled vehicle. Considering the coupled vehicle-driver system, a model of the human or robot driver control behaviour may be

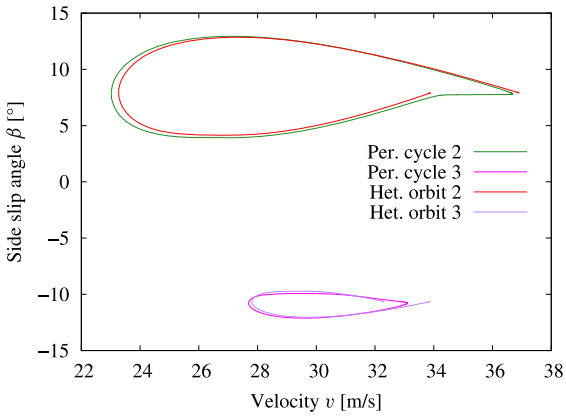

Fig. 13 Trajectories of periodic solutions for $\delta_F = -3°$ and corresponding heteroclinic orbits

included to analyse the dynamics of the closed-loop system.

Acknowledgements The authors acknowledge TU Wien Bibliothek for financial support through its Open Access Funding Program.

Author contributions J.E. and M.P. formulated the mechanical modelling and carried out experiments. A.S. carried out the numerical and analytical investigations. All authors reviewed the manuscript.

Funding Open access funding provided by TU Wien (TUW). The authors received no funding for this research.

Data availability No datasets were generated or analysed during the current study.

Declarations

Conflict of interest The authors declare that they have no conflict of interest.

Appendix: Numerical calculation of the stationary, periodic and heteroclinic solutions

Since most of the obtained periodic solutions are numerically very unstable, a robust solver for the boundary value problems had to be applied. In this study, the multiple shooting algorithm Boundsco [9], was used. For very long periodic solutions several thousand grid points had to be used to obtain solutions.

Since the parameters δ_F and M_R are assumed to vary along the PS-curve for $\rho = 50$m in the handling diagram Fig. 4, the steady-state solutions along the handling diagrams had to be calculated together with the stationary solutions on branch 2, the periodic and heteroclinic solutions.

To obtain the stationary solutions on Branch 2 in Fig. 3, a system for two state vectors $\boldsymbol{y}_1$ and $\boldsymbol{y}_2$ and the control variables δ_F and M_R had to be solved by a Newton iteration: Both vectors $\boldsymbol{y}_i$ satisfy (7), the point $\boldsymbol{y}_1$ on the powerslide branch has to satisfy the additional relation $v_1 = \rho\dot{\psi}_1$; for the point $\boldsymbol{y}_2$ on Branch 2 there is no such restriction. The equations for $\boldsymbol{y}_1$ guarantee that the control variables vary on the powerslide branch shown in Fig. 4.

For the periodic and heteroclinic solutions the parameters and steady states were introduced as free parameters, that is state variables y_i satisfying the trivial differential equations $\dot{y}_i = 0$. The steady-state conditions (7) and the relation $v = \rho\dot{\psi}$ for the steady states were prescribed as boundary conditions at the left endpoint.

Since the period of solutions of autonomous systems is unknown and the numerical method requires a fixed integration interval, the unknown time interval $t \in [0, T]$ was transformed to the fixed interval $\tau \in [0, 1]$ with $t = T\tau$, where T was treated as further free parameter and the right-hand side of the original differential equations was multiplied by T. To fix the phase of the periodic solutions, the additional boundary condition

$$\dot{v}(0) = 0$$

was prescribed.

In order to efficiently calculate families of periodic solutions, a local adaption of the continuation algorithm Hom [14], with automatic step size control and tangential updating was used. By Hom the direction of the solution path is selected by specifying an additional boundary condition $y_k(0) = \eta$, where the vector

$\boldsymbol{y}$ contains all unknown variables and the index k is chosen such that relative variation in the component $y_k(0)$ during the previous steps is maximized. With Hom it is easily possible to pass LPCs.

For the calculation of the heteroclinic orbits also the algorithm Boundsco was applied. The unknown endpoints P_1 and P_2 on the critical manifold $\mathscr{M}_c$ were regarded as free parameters satisfying the conditions (7) for P_1 and (7a-c) for P_2. Since both points lie on the critical manifold, the condition (7d) for both points would be linearly dependent.

A further set of free parameters was related to the steady-state values along the curve in the handling diagram, which have to satisfy the additional conditions

$$v = \rho\dot{\psi} \qquad \text{and } |\sigma_{yF}| = \sigma_{F,\text{sat}}.$$

In order to guarantee the proper convergence of the heteroclinic orbit towards the steady-state points P_1 and P_2

$$\lim_{t\to-\infty} \boldsymbol{y}(t) = P_1, \qquad \lim_{t\to\infty} \boldsymbol{y}(t) = P_2,$$

the infinite integration interval was truncated to a sufficiently large interval $[T_1, T_2]$ with $T_1 < 0 < T_2$ and asymptotic boundary conditions [8], were stated: Since along $\mathscr{M}_c$ one eigenvalue vanishes, one is unstable and two are stable, it had to be ensured that

$$\boldsymbol{y}(T_1) \in \mathscr{M}^u(P_1),$$
$$\boldsymbol{y}(T_2) \in \mathscr{M}^s(P_2),$$

where $\mathscr{M}^u(P_i)$ and $\mathscr{M}^s(P_i)$ denote the unstable and stable invariant manifolds at the points P_i, respectively. These can locally be approximated by the corresponding eigenspaces, spanned by the eigenvectors with positive and negative real parts, respectively.

Let $\mathbf{A}_i$ denote the Jacobian of the differential equation at P_i and λ_{ij} and $\boldsymbol{v}_{ij}$ the corresponding left eigenvalues and eigenvectors, respectively:

$$\mathbf{A}_i^{\mathrm{T}}\boldsymbol{v}_{ij} = \lambda_{ij}\boldsymbol{v}_{ij},$$

for $i \in \{1, 2\}$ and $j \in \{1, 2, 3, 4\}$. Then the (linearized) conditions (1) can be written as

$$\boldsymbol{v}_{1cs}^{\mathrm{T}}(\boldsymbol{y}(T_1) - P_1) = 0,$$
$$\boldsymbol{v}_{2cu}^{\mathrm{T}}(\boldsymbol{y}(T_2) - P_2) = 0.$$

Here, $\boldsymbol{v}_{1cs}$ [$\boldsymbol{v}_{2cu}$] are the left eigenvectors for the eigenvalues with non-positive and non-negative real parts at P_1 [P_2], respectively.

Since it would be very expensive to solve the eigenvalue problems at every iteration, it is usually more efficient to select T_1 and T_2 large enough and calculate the eigenvectors just for one point on the critical manifold.

Finally, also a phase condition for the solution had to be stated, where again

$$\dot{v}(0) = 0.$$

was used. As an initial guess for the heteroclinic solution, the fast segment of a periodic solution with a long period was used.

References

1. Abdulrahim, M.: On the dynamics of automobile drifting. SAE paper no 2006-01-1019 pp 169–178 (2006)
2. Della Rossa, F., Mastinu, G., Piccardi, C.: Bifurcation analysis of an automobile model negotiating a curve. Veh. Syst. Dyn. **50**(10), 1539–1562 (2012). https://doi.org/10.1080/00423114.2012.679621
3. Edelmann, J., Plöchl, M.: Handling characteristics and stability of the steady-state powerslide motion of an automobile. Regul. Chaot. Dyn. **14**(6), 682–692 (2009). https://doi.org/10.1134/S1560354709060069
4. Edelmann, J., Plöchl, M., Lugner, P., et al.: Investigations on the powerslide of automobiles. In: Proceedings of AVEC 2008 (2008)
5. Edelmann, J., Eberhart, M., Steindl, A., et al.: Post-critical behaviour of the powerslide motion. Submitted to Vehicle System Dynamics (2024)
6. Fenichel, N.: Geometric singular perturbation theory for ordinary differential equations. J. Differ. Equ. **31**, 53–98 (1979). https://doi.org/10.1016/0022-0396(79)90152-9
7. Kuehn, C.: Multiple Time Scale Dynamics, 1st edn. Springer, Cham (2015). https://doi.org/10.1007/978-3-319-12316-5
8. Lentini, M., Keller, H.B.: Boundary value problems on semi-infinite intervals and their numerical solution. SIAM J. Numer. Anal. **17**(4), 577–604 (1980). https://doi.org/10.1137/0717049
9. Oberle, H.J., Grimm, W., Berger, E.: BNDSCO, Rechenprogramm zur Lösung beschränkter optimaler Steuerungsprobleme. Benutzeranleitung M 8509, Techn. Univ. München (1985)
10. Pacejka, H.B.: Simplified analysis of steady-state turning behaviour of motor vehicles. Part 1. handling diagrams of simple systems. Veh. Syst. Dyn. **2**, 161–172 (1973)
11. Pacejka, H.B.: Simplified analysis of steady-state turning behaviour of motor vehicles. Part 2. stability of the steady-state turn. Veh. Syst. Dyn. **2**, 173–183 (1973)
12. Pacejka, H.B.: Tire and Vehicle Dynamics. Butterworth-Heinemann, Oxford (2012)
13. Pauwelussen, J.: Axle characteristics and vehicle limit cycle behaviour. Veh. Syst. Dyn. (2024). https://doi.org/10.1080/00423114.2024.2322487

14. Seydel, R.: A continuation algorithm with step control. In: Numerical Methods for Bifurcation Problems. ISNM 70. Birkhäuser (1984)
15. Steindl, A., Edelmann, J., Plöchl, M.: Limit cycles at oversteer vehicle. Nonlinear Dyn. **99**, 313–321 (2020). https://doi.org/10.1007/s11071-019-05081-8
16. Steindl, A., Edelmann, J., Plöchl, M.: Influence of tyre characteristics on periodic motions for an understeering vehicle. PAMM **22**(1), e202200289 (2023). https://doi.org/10.1002/pamm.202200289
17. Velenis, E., Katzourakis, D., Frazzoli, E., et al.: On the dynamics of automobile drifting. In: Proceedings of AVEC 2010 (2010)